Experimental and Theoretical Studies on X-ray Plane Wave Images of a Dislocation in the Laue Case *

H. Ishida **
Institute of Engineering Research, University of Tokyo

N. Miyamoto ***, T. Ishikawa, and K. Kohra ****
Department of Applied Physics, Faculty of Engineering, University of Tokyo

Z. Naturforsch. **37 a**, 650–659 (1982); received May 19, 1982

Dedicated to Prof. Hildebrandt on the occasion of his 60th birthday

Plane wave images of a dislocation in a silicon crystal were observed with ($\bar{4}04$) diffraction of MoKα_1 over a wide angular range. The fine structures consisting of five kinds of sub-images and their angular dependences were well simulated by the wave theory taking into account the finite angular spread and polarization states of the incident beam. The mechanism of the image formation is studied in terms of interbranch scattering, Eikonal theory and kinematical diffraction.

1. Introduction

Recently, plane wave X-ray topography has commenced to be utilized for studies of individual defects such as dislocations [1–4] and point defects [5] as a complementary method to spherical wave topography, the representative ones being Lang's traverse and section topography [6]. Concerning the formation mechanism of the defect images by spherical wave topography, dislocation images in a section topograph were studied [7] by comparing them with images simulated by the wave theory [8]. In the present study, a detailed analysis of the formation mechanism of plane wave images of a dislocation will be presented.

The analysis of dislocation images in the plane wave topography is expected to give a more detailed information about the image formation mechanism and the behavior of X-rays around the defects. However, the experimental observation of the plane wave images requires an extremely high angle-resolution, so that most previous studies seem to be unsatisfactory.

In the present study, plane wave topographs of a dislocation in a silicon crystal in the Laue case will be shown and compared with theoretical calculations. In order to obtain as much information as possible, the experimental observations and the calculations were made in the following way: A series of topographs was taken over a wide angular range around the Bragg peak at a small angular intervals with high angular precision. The observations were made with a (440) reflection of MoKα_1. The higher order reflection gives a broad image so that the fine structures could be easily separated, and MoKα_1 enabled us to observe the interference between both strongly and weakly absorbing wavefields in contrast to CuKα_1. Thus, fine structures of the dislocation images and their drastic change with diffraction conditions were observed.

On the other hand, image calculations by the wave theory were made for conditions corresponding to the experiment, i.e. with a finite angular spread and both polarization states of the incident beam. The fine structures and their drastic changes observed were quite well reproduced by the calculations.

From a detailed comparison of the calculated and observed fine structures, some sub-images or fine structures were explained by the Eikonal theory [9] as due to diffraction in a weakly distorted region, some sub images by the interbranch scatterning [10] as due to diffraction in an intermediately distorted

Reprint requests to Prof. K. Kohra, National Laboratory for High Energy Physics, Oho-machi, Tsukuba-gun, Ibaraki 305, Japan.

* The theoretical part of this paper is based in part on a Doctoral thesis of H. Ishida submitted to the University of Tokyo, 1978 (in Japanese).

** Present address: Shimadzu Corporation, Kuwabara-cho, Nisinokyo, Nakagyo-ku, Kyoto 604, Japan.

*** Present address: Kyoto Ceramics Ltd. Kokubu-shi, Kagoshima 899-43, Japan.

**** Present address: National Laboratory for High Energy Physics, Oho-machi, Tsukuba-gun, Ibaraki 305, Japan.

0340-4811 / 82 / 0700-0650 $ 01.30/0. — Please order a reprint rather than making your own copy.

region and some sub-images by kinematical diffraction as due to diffraction in a heavily distorted region.

2. Experimental

A double crystal arrangement of parallel setting was used to take ($\bar{4}04$) topographs of a silicon single crystal with MoKα_1 radiation, as shown in Figure 1. For the first crystal, asymmetric diffraction [11] was used with an asymmetry factor

$$b = \sin(\theta_B + \alpha)/\sin(\theta_B - \alpha) = 25\,.$$

Here, α is the angle between crystal surface and diffracting plane and θ_B is the Bragg angle. The angular spread of the beam incident on the second crystal is estimated to be 0.16 seconds in arc, one fifth of the angular range of selected diffraction in the symmetric case, 0.78 seconds in arc, which is used for the specimen crystal. The horizontal cross section of the beam was broadened by asymmetric diffraction to approximately 4 mm.

The spatial resolutions in the vertical and horizontal directions are given by

$$\Delta r_v = f_v L_3/(L_1 + L_2) \qquad (1a)$$

and

$$\Delta r_h = L_3 \tan\theta_B(\delta\lambda/\lambda)\,, \qquad (1b)$$

respectively. Here, L_1, L_2 and L_3 are the source-monochromator, monochromator-specimen and specimen-photographic plate distances, respectively, f_v is the vertical size of the X-ray source and $\delta\lambda/\lambda$ the wavelength spread.

In the experiment, the following values were used: $L_1 = 30$ cm, $L_2 = 25$ cm, $L_3 = 1$ cm, apparent vertical and horizontal sizes of the X-ray source 0.09 and 0.07 mm, respectively, and width of MoKα_1 $\delta\lambda/\lambda \cong 4 \times 10^{-4}$. The vertical and horizontal resolutions are estimated to be 1.6 μm by inserting these values into (1a) and (1b).

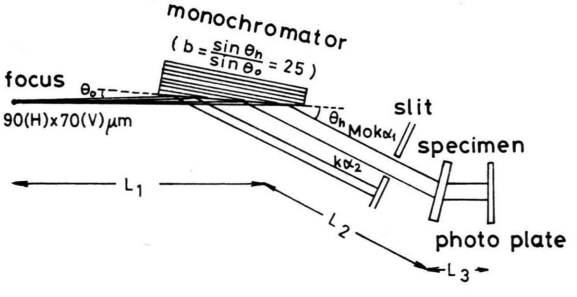

Fig. 1. Experimental arrangement.

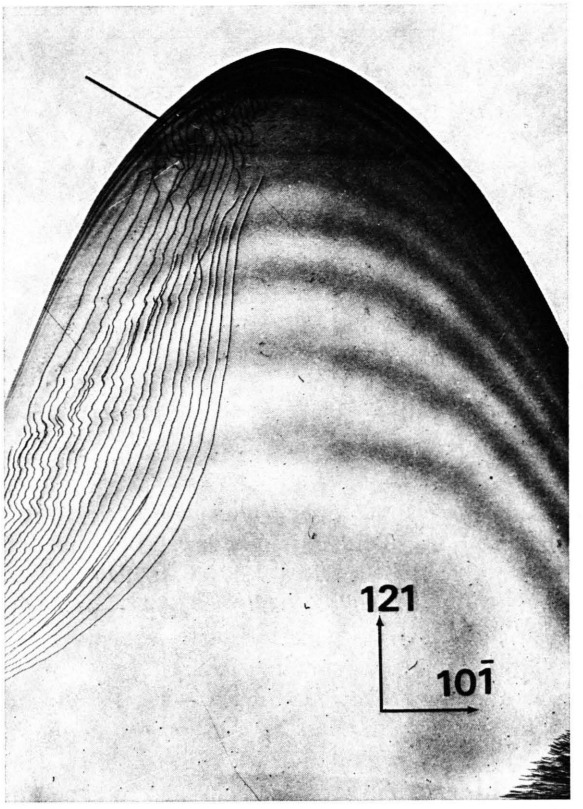

Fig. 2. Lang topograph of the whole of specimen. $h = (20\bar{2})$, MoKα_1 (courtesy of Dr. J. Chikawa).

The specimen was a ($1\bar{1}1$) silicon wafer which had been used by Dr. J. Chikawa and his co-workers [12]. A Lang topograph of the specimen crystal is reproduced in Figure 2. A dislocation in the specimen indicated by an arrow was studied in the present work. Figure 3 shows the geometrical configuration of the part of the specimen containing this dislocation and Fig. 4 the corresponding Lang topograph. In this area, the incident surface is parallel to ($1\bar{1}1$) within a few minutes in arc, while the exit surface is inclined at 3.2° to the incident surface. The crystal thickness varies almost linearly from 174 μm to 206 μm along the [121] direction. The dislocation to be studied lies on the plane parallel to the incident surface at a depth of 90 μm. The dislocation line is curved and the angle between its tangential direction and [10$\bar{1}$] varies from 50° to 80°. The Burgers vector of the dislocation was determined to be $-1/2[10\bar{1}]$ [13].

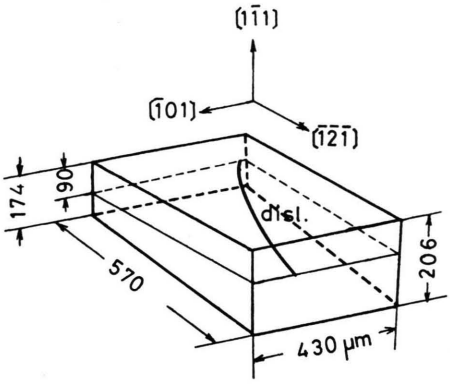

Fig. 3. Configuration of the observed area of the specimen.

Plane wave topographs were taken at seven angular positions of the specimen crystal around the Bragg peak: $W=-2.1$, -1.4, 0.0, 0.7, 1.4, 2.1 or $\delta\theta=0.8''$, $0.56''$, $0.0''$, $-0.3''$, $-0.56''$, $-0.8''$ and $-1.4''$, where W is a parameter representing the deviation of the incident angle from the exact Bragg angle and is normalized so that $-1<W<1$ indicates the angular range of selected diffraction of the crystal. Before taking each topograph, the stability of the arrangement was checked by monitoring the diffracted intensity for several tens of minutes. Furthermore, the drift during exposure was corrected by monitoring the beam transmitted through the photographic plate.

A rotary anode X-ray generator was operated at 40 kV and 7 mA. Nuclear plates Ilford L4 were used for the photographs. The exposure time was 2—8 hours according to the diffraction conditions.

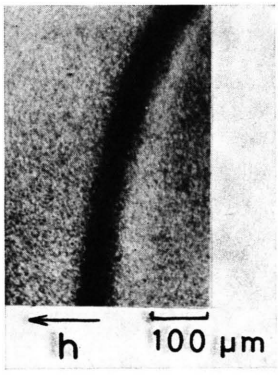

Fig. 4. Lang traverse image of a dislocation. $\boldsymbol{h}=(\bar{4}04)$, MoK$\alpha_1$, $\boldsymbol{b}=-1/2[\bar{1}01]$.

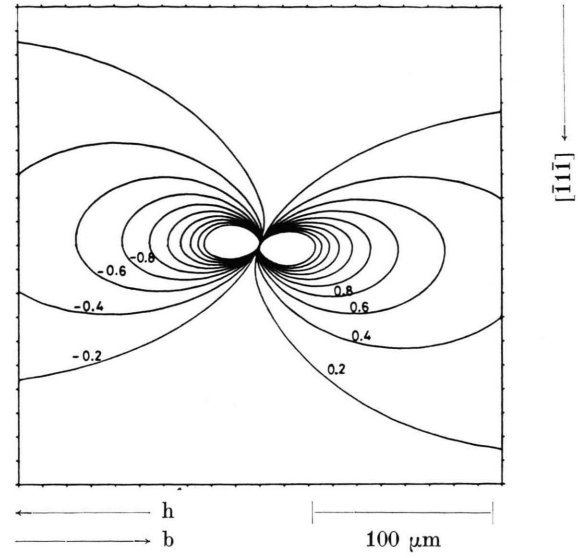

Fig. 5. Calculated contour map of the strain $\beta_h'=-1/k\cdot\partial/\partial s_h(\boldsymbol{h}\cdot\boldsymbol{u})$ around a dislocation in the plane of incidence. Units: $|C\chi_h|\cdot\boldsymbol{h}=(\bar{4}04)$, MoK$\alpha_1$, $\boldsymbol{b}=-1/2[\bar{1}01]$.

3. Calculations

The dislocation images were calculated using Takagi's Eq. [8] in the same way in principle as in previous studies [14] but with the improvement that the finite angular spread and the polarization states of the exploring beam were taken into account corresponding to the experimental conditions.

The dislocation of interest is curved, but the lattice displacement was calculated using anisotropic elasticity theory for a straight dislocation [15] which makes a 70° angle with [10$\bar{1}$]. Figure 5 shows a contour map of the strain $\beta_h'=-(\partial/\partial s_h)(\boldsymbol{h}\cdot\boldsymbol{u})/k$ around the dislocation thus derived, k being the wave number of the incident X-rays, $\boldsymbol{h}=(\bar{4}04)$ the diffracting vector of $(\bar{4}04)$ and s_h an oblique coordinate along the wave vector $\boldsymbol{k}_h$ of the diffracted beam.

The size of the vertical step for integration was one fiftieth of the extinction distance, 54 μm. The computation time was approximately 3 minutes per one diffraction condition.

4. Observations and Comparison with Calculations

Figure 6 shows observed and calculated topographs at various diffraction conditions. The agreement on the whole is good. On both sides of the calculated images intensity variations exist, espe-

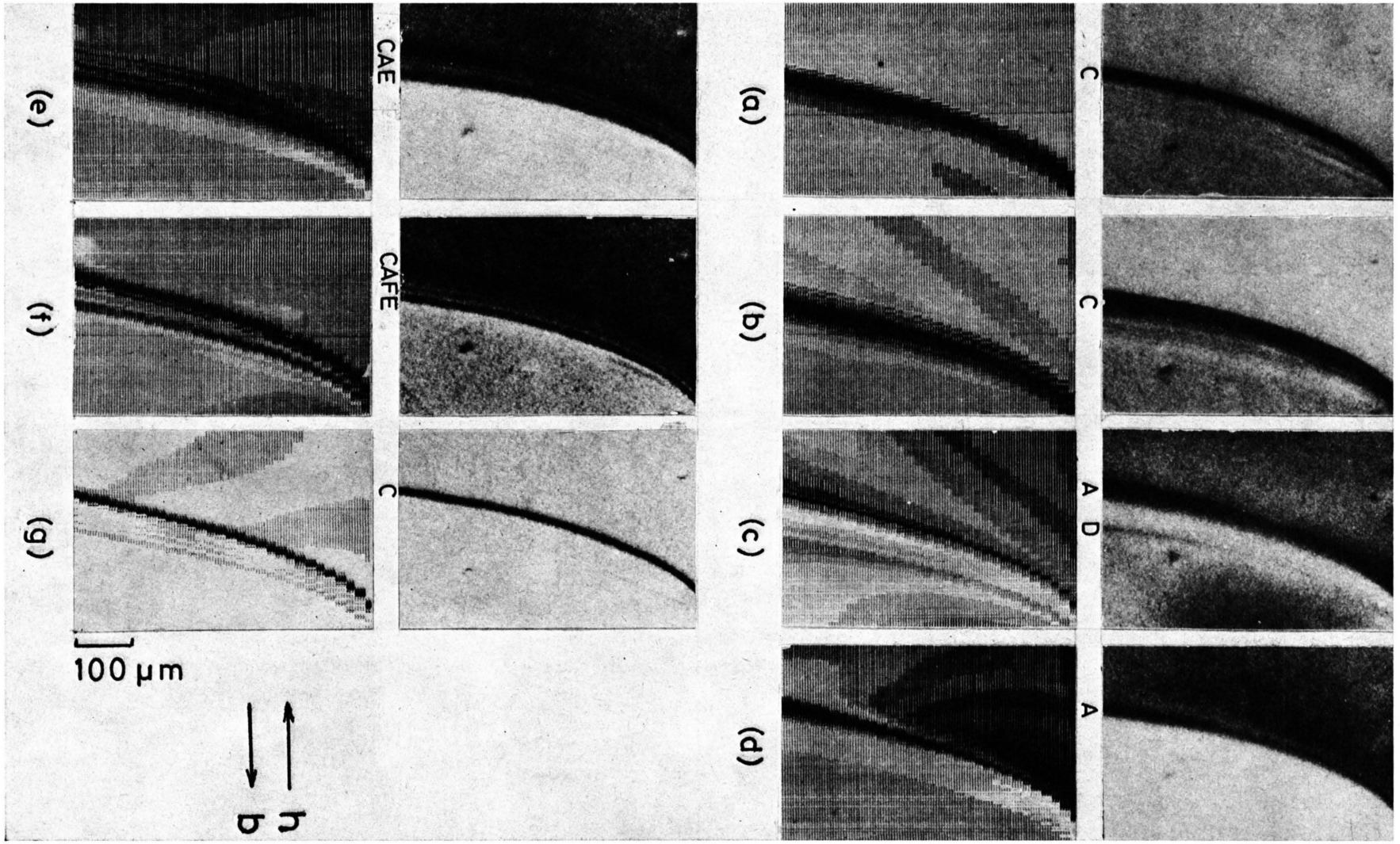

Fig. 6. Observed (upper) and calculated (lower) dislocation images taken by plane wave topography at various angular positions: (a) $W=-2.1$ ($\delta\theta=0.8''$), (b) $W=-1.4$ ($\delta\theta=0.56''$), (c) $W=0.0$ ($\delta\theta=0.0''$), (d) $W=0.7$ ($\delta\theta=-0.3''$), (e) $W=1.4$ ($\delta\theta=-0.56''$), (f) $W=2.1$ ($\delta\theta=-0.8''$) and (g) $W=3.6$ ($\delta\theta=-1.4''$), $\delta\theta$ being the deviation of the incident angle from the exact Bragg angle.

cially in (b), (c) and (d), which correspond to the equal-thickness fringes modified strongly by the lattice distortion [13].

Figure 7 shows calculated intensity profiles of the dislocation images which were made along the horizontal direction at the bottoms of Fig. 6. A_d and B_d are projections of A_d' and B_d' onto the photographic plate, where A_d' and B_d' are intersections of the wave vectors $\boldsymbol{k}_0$ and $\boldsymbol{k}_h$, originating at the dislocation, with the exit surface of the specimen. The profiles consist of sub-peaks corresponding to sub-images or fine structures in the dislocation images and change drastically with the diffraction conditions.

In Fig. 6, the change of the dislocation images with the diffraction conditions is asymmetrical with respect to the Bragg peak and is more complex on the side $W>0$ than on the side $W<0$. The corresponding facts are confirmed in Fig. 7. In Fig. 8, three of the observed images are enlarged where the fine structures observed agree well with the corresponding intensity profiles (Fig. 7) except for a few points: a grey-white-grey contrast is additionaly observed on the right side of sub-image C in Fig. 8(a) and sub-image F consists of two peaks.

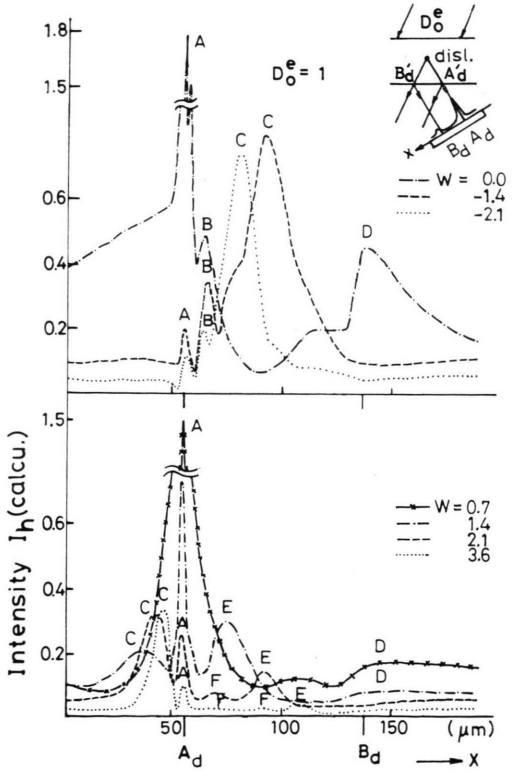

Fig. 7. Intensity profiles of the calculated images of Fig. 6 taken at the bottom of the photographs along the horizontal direction.

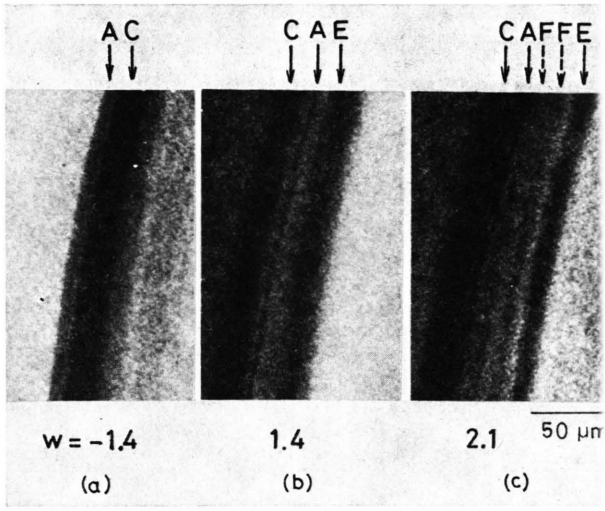

Fig. 8. (a), (b) and (c) are enlargements of the upper photographs of (b), (e) and (f) of Fig. 6, respectively.

Let us now study some details of the observed images and intensity profiles in comparison with the calculated ones.

In Fig. 6(a) ($W=-2.1$), the image consists mainly of a single sharp and black line, C. In Fig. 6(b) ($W=-1.4$), the black line C becomes broader and on the right side a weak white line appears. In Fig. 6(c), where the Bragg condition is satisfied exactly, the sub-image C disappears, while a rather broad line A and a narrow weak line D are observed. In Fig. 6(d) ($W=0.7$), the line D disappears and the intensity contrast between both sides of the dislocation image is strongest, together with Fig. 6(e), probably because the lattice buckling is detected most sensitively in these regions of diffraction conditions. In Fig. 6(e) ($W=1.4$), two broad black lines, C and E appear, while A still remains between them as a very sharp line, 3 μm in width. In Fig. 6(f) ($W=2.1$), C moves toward A, which remains at a fixed position, and E moves away from A and two lines F appear. The line F, on the other hand, does not appear as a double line but a single line in the calculation. In Fig. 6(g) ($W=3.6$), the dislocation image becomes again a simple sharp black line C as in Fig. 6(a).

In the calculated profiles at $W=0.0$, -1.4 and -2.1 an extra peak B is seen, which is not ob-

served. This probably results from the difficulty in observing B separately because of its small summit on the tail part of peak A ($W = 0.0$) or C ($W = -1.4$ and -2.1), and further because of the overexposure at $W = -1.4$.

5. Analysis of Fine Structures in Dislocation Images

Figure 9 shows intensity maps of the wave fields of diffracted beams around the dislocation in a plane of incidence, calculated under diffraction conditions

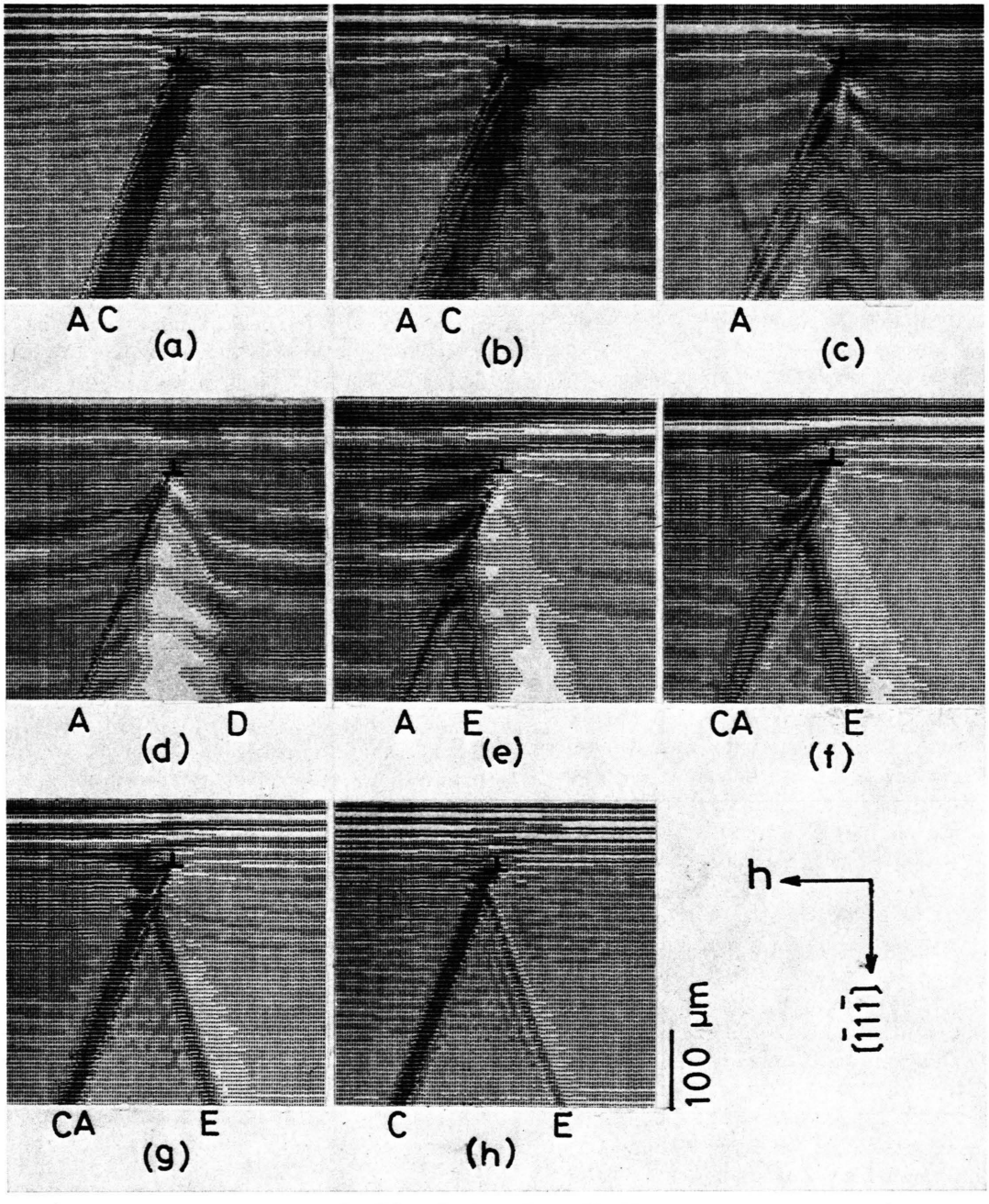

Fig. 9. Intensity distributions around a dislocation in a plane of incidence at various W-values: (a) $W = -2.1$, (b) $W = -1.4$, (c) $W = -0.7$, (d) $W = 0.0$, (e) $W = 0.7$, (f) $W = 1.4$, (g) $W = 2.1$ and (h) $W = 3.6$. $\boldsymbol{h} = (\bar{4}04)$, MoK$\alpha_1$, $\boldsymbol{b} = -1/2[\bar{1}01]$.

corresponding to those in Fig. 6. In the maps all the sub-images discussed in the former section are indicated except B and F. The calculations made by the wave theory reproduce well the observed sub-images, as shown in Figs. 6 and 9. However, as is well known, the physical meaning of image formation is not clear from the calculations by the wave theory.

On the other hand, the Eikonal theory has been successfully used for the study of weakly distorted crystals [16—18]. In the Eikonal theory, the physical concepts such as two wave fields and their respective beam paths, which are established for a perfect crystal, remain to be valid. In Fig. 10, the trajectories of rays around the dislocation calculated by the Eikonal theory for σ-polarization are shown, which correspond to the paths of the energy flow of the wave fields consisting of o- and h-waves.

In the following section, some of the sub-images (D and E) will be explained by the Eikonal theory. The other sub-images, which are not explained by the Eikonal theory, will be analyzed in terms of interbranch scattering (C), kinematical diffraction (A) and interference effect (F).

5.1. Sub-images Explained by the Eikonal Theory, D and E

In the intensity profiles of Fig. 7, peak D is seen only on the side of $W>0$. For any diffraction condition, $W=0.7$, 1.4 or 2.1, the intensity ratio between the left and right sides of peak D is approximately 1:2. This ratio can be explained by the Eikonal theory where the ratio is given as the intensity ratio of wave field 1 to the sum of the two wave fields. In Fig. 10(e), (f) and (g) only wave field 1 exists on the left side of D, while on the right side of D two wave fields always exsist.

Peak E, which is observed in Figs. 6(e) and (f), can be explained also by the Eikonal theory. As seen in Fig. 10(e), (f) and (g), peak E appears as the result of convergence of the rays belonging to the wave field 2. At the position S this convergence of the beam flux contributing to E begins, and the direction of the beam flux changes with diffraction condition in the same way as in the maps of wave fields calculated by the wave theory (Figs. 9(e), (f) and (g)). The separation of the images E and C is not due to interbranch scattering but is rather due to the fact that the beam convergence of wave field 2 happens to start near the image C.

5.2. Sub-image Explained by the Interbranch Scattering, C

The Eikonal theory cannot explain the following points of peak C observed and calculated by the wave theory:

(i) The peak C is of very high intensity on the side $W<0$.

(ii) The peak C separates from A on the side $W>0$.

A possible interpretation of the formation of peak C is that, when one of the wave fields propagating along the $\boldsymbol{k}_0$-direction in the perfect region of the crystal approaches the dislocation, the diffraction condition is locally satisfied and another wave field is excited, that is, interbranch scattering [10] takes place. The excited wave field changes its propagation direction from the direction along the diffracting plane to the $\boldsymbol{k}_h$-direction.

The high intensity of peak C in Fig. 7 on the side $W<0$ indicates that the rate of wave field 1 exciting wave field 2 is high. Otherwise, another peak labelled D in Fig. 10(b) would have been observed. On the other hand, the rate of wave field 2 exciting wave field 1 on the side $W>0$ must be low. Nevertheless, interbranch scattering is equally important on the $W>0$ side for the interpretation of image C where C is separated from A.

Next, we compare the experimental width of image C (Fig. 6) with the calculated one (Figure 7). The result is shown in Figure 11. At $W=-2.1$, -1.4, 2.1 and 3.6 the experimental values are 19, 27, 16, and 10 μm, respectively, while the calculated widths are 16, 20, 17 and 10 μm. If we assume the image width to be given by

$$H=\frac{\boldsymbol{h}\cdot\boldsymbol{b}}{2}\frac{\Lambda}{|W|}, \tag{2}$$

where Λ is the extinction distance and $\boldsymbol{b}$ the Burgers vector, this explains well the experimental as well as the calculated values. The applicability of (2) is confined to off-Bragg diffraction conditions ($|W|>1$). This formula is comparable with the expression for the width of dislocation image in the Lang topograph [19] given by

$$H'=\frac{\boldsymbol{h}\cdot\boldsymbol{b}}{2}\Lambda. \tag{3}$$

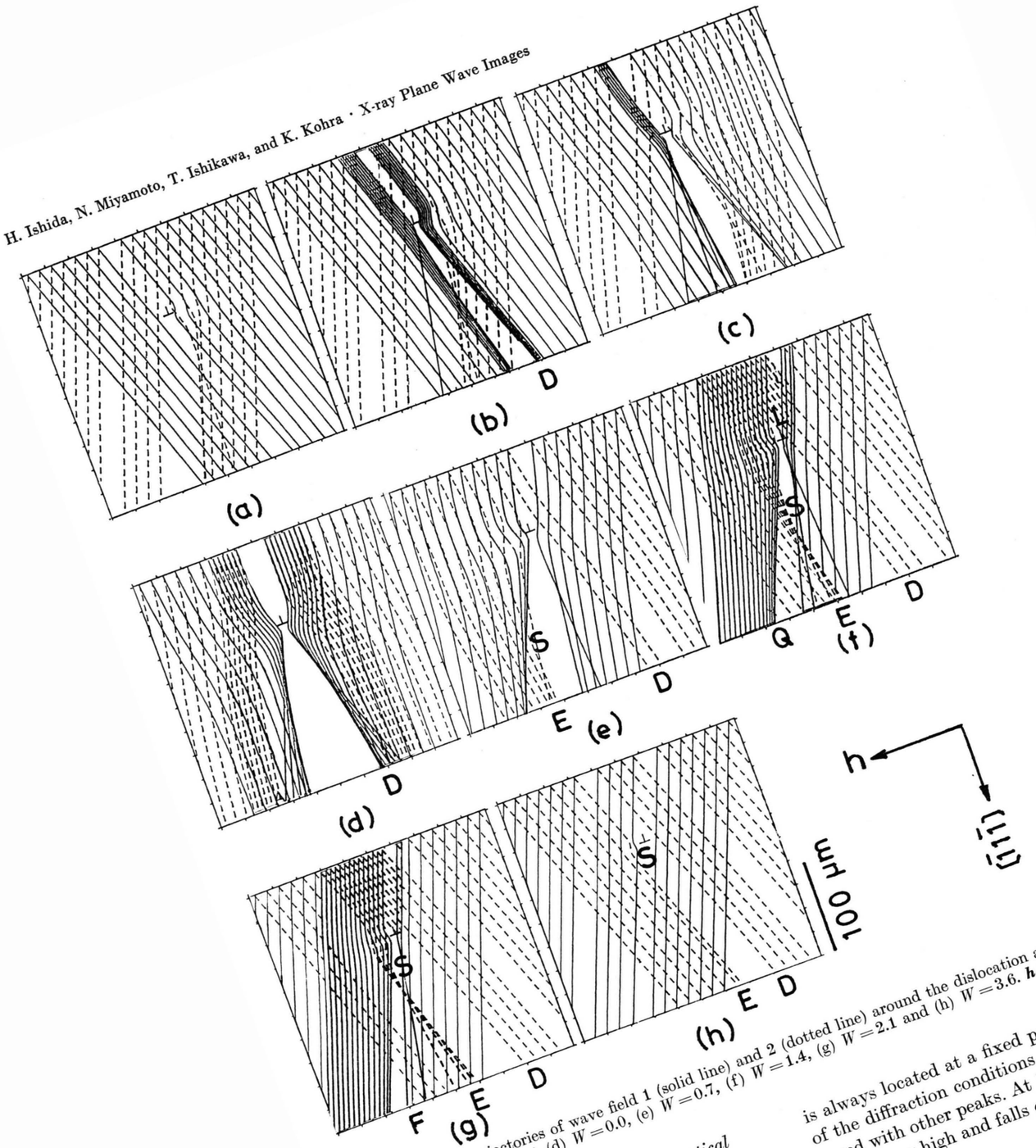

Fig. 10. Energy trajectories of wave field 1 (solid line) and 2 (dotted line) around the dislocation at (a) $W=-2.1$, (b) $W=-1.4$, (c) $W=-0.7$, (d) $W=0.0$, (e) $W=0.7$, (f) $W=1.4$, (g) $W=2.1$ and (h) $W=3.6$. $\boldsymbol{h}=(\bar{4}04)$, MoK$\alpha_1$, $\boldsymbol{b}=-1/2[\bar{1}01]$.

5.3. *Sub-image Explained by the Kinematical Diffraction, A*

Peak A is produced by the diffraction in the immediate neighbourhood of the dislocation core and is always located at a fixed position independently of the diffraction conditions. It is very sharp compared with other peaks. At $W=0.0$ the peak intensity is very high and falls of rapidly with deviation

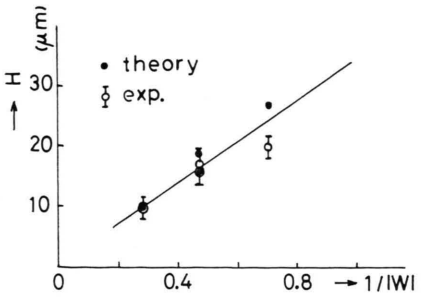

Fig. 11. Dependence of the width of the off-Bragg angle image of the dislocation on the Bragg departure or W-value. The line is drawn from (3).

from the exact Bragg condition. This image is separated from the other peaks at $W=1.4$ and 2.1.

If we assume kinematical diffraction for the neighbourhood of a dislocation, the transmitted and diffracted waves incident in the neighbourhood separate after diffraction and flow independently along $\boldsymbol{k}_0$ and $\boldsymbol{k}_h$, respectively. On this assumption, peak A is formed by the separated $\boldsymbol{h}$-wave so that it is always located at a fixed position.

The energy density of the wave field entering the neighbourhood determines the dependence of the peak height of A on the diffraction condition. At the exact Bragg condition, it seems that the energy flow of wave field 1 is attracted by the dislocation as shown in Fig. 10(d), while wave field 2 is repelled. Therefore, the amount of wave field 1 approaching the dislocation is much bigger than that of wave field 2. The direction of the energy flow of wave field 1 changes on approaching the dislocation, so that the intensity of the resultant image is given by the sum of the intensities of diffracted beams excited in the neighbourhood of the dislocation by various incident directions. Thus, peak A is a kind of integrated image showing high intensity.

When the incident angle deviates from the Bragg condition, the energy incident in the neighbourhood of the dislocation is restricted, because it becomes harder for the energy flow to be curved to a sufficient degree by the same strain gradient in the dislocation neighbourhood and to converge into the dislocation with high intensity.

5.4. Peak F

Peak F results probably from interference of some two wave fields. There are differences between calculation and observation in the following points:

(i) Peak F has a fairly strong contrast but is not so distinct in the calculation.

(ii) There are two peaks F observed at $W=2.1$, while only one appears in the calculation.

As a probable explanation, the strain field in the neighbourhood of the dislocation might be strongly modified by the existence of impurities.

6. Discussions

In the present study, the fine structures of the dislocation images and their dependence on the diffraction condition are more distinctly observed even at far-off Bragg conditions than in the previous studies [1, 2]. Such improvements in quality of the observed images are due to the use of higher order reflections of harder X-rays, $(\bar{4}04)$ of MoKα_1, as was mentioned in introduction.

On the other hand, a good agreement between observations and calculations is achieved in the present study by adopting the conditions of the incident beam having a finite angular spread and polarization states corresponding to the experimental conditions. In the case of an infinitely narrow angular spread for the incident beam, as usually used for the calculations of plane wave images [2, 3, 20], the calculated images reveal much more complicated fine structures with higher contrast than those observed or calculated with finite angular spread of the incident beam.

We have applied plane wave topography to studies on various kinds of strain fields due to small point-like defects, surface stress relaxation and impurity atoms attached to a dislocation core, the results of which will be reported elsewhere in the near future.

Further, by using synchrotron radiation, high intensity exploring beams of narrow spreads in wavelength as well as angle can be obtained with a $(+n, +m)$ double crystal monochro-collimator system. Thus plane wave topography will be applied to any kind or any lattice spacing of crystals [21] as a powerful method for characterization of single crystals.

Acknowledgements

The authors wish to express their thanks to Dr. J. Chikawa for allowing them to use the specimen

crystal. They are also the thankful to Mr. K. Murai for providing a dislocation-free silicon single crystal for the monochromator and to Drs. H. Hashizume, M. Ando and T. Matsushita for their valuable discussions and to Mrs. M. Isogai, K. Ohara and T. Ozaki for their helps in taking topographs.

[1] M. Renninger, Z. Naturforsch. **19a**, 783 (1964); M. Renninger, Z. ang. Phys. **19**, 22, 34 (1965)
[2] S. Takagi, K. Ishida, and A. Ootuka, J. Phys. Soc. Japan. **45**, 1067 (1978); K. Ishida, A. Ootuka, and S. Takagi, Phil. Mag. **A43**, 935 (1981).
[3] H. Ishida, N. Miyamoto, and K. Kohra, J. Appl. Cryst. **9**, 240 (1976).
[4] R. Bubakova and Z. Sourek, phys. stat. sol. (a), **35**, 55 (1976).
[5] M. Renninger, J. Appl. Cryst. **9**, 178 (1976).
[6] A. R. Lang, J. Appl. Phys. **29**, 527 (1958).
[7] F. Balibar and A. Authier, phys. stat. sol. **21**, 413 (1967).
[8] S. Takagi, Acta Cryst. **15**, 1311 (1962); S. Takagi, J. Phys. Soc. Japan. **26**, 1239 (1969); D. Taupin, Bull. Soc. Franc. Miner. Crist. **87**, 469 (1964).
[9] N. Kato, J. Phys. Soc. Japan. **18**, 1785 (1963); **19**, 67,971 (1964); P. Penning and D. Polder, Philips Res. Pepts. **16**, 419 (1961).
[10] A. Authier, F. Balibar, and Y. Epelboin, phys. stat. sol. **41**, 225 (1970).
[11] M. Renninger, Z. Naturforsch. **16a**, 1110 (1961); K. Kohra, J. Phys. Soc. Japan **17**, 589 (1962).
[12] J. Chikawa, J. Cryst. Growth **24/25**, 61 (1974).
[13] H. Ishida, J. Appl. Cryst. **13**, 58 (1980).
[14] Y. Epelboin, Acta Cryst. **A31**, 591 (1975); Y. Epelboin, Acta Cryst. **A35**, 38 (1979).
[15] J. W. Steeds, Anisotropic Elasticity Theory of Dislocations, Oxford, London 1973.
[16] N. Kato and Y. Ando, J. Phys. Soc. Japan **21**, 964 (1966).
[17] M. Hart, Z. Physik **189**, 269 (1966).
[18] J. R. Patel and N. Kato, Appl. Phys. Letters, **13**, 40 (1968); N. Kato and J. R. Patel, J. Appl. Phys. **44**, 965 (1973); J. R. Patel and N. Kato, J. Appl. Phys. **44**, 971 (1973).
[19] A. R. Lang and M. Polcarova, Proc. Roy. Soc. **A285**, 297 (1965).
[20] T. Bedynska, R. Bubakova, and Z. Sourek, phys. stat. sol. (a), **36**, 509 (1976).
[21] J. F. Petroff, M. Sauvage, P. Riglet, and H. Hashizume, Phil. Mag. **A42**, 319 (1980).